Chapter 3

In-situ Growth of CuO Nanoflakes on Graphitic Carbon Nitride Sheets: An Electro-active Interface for Electrocatalytic Oxidation of Riboflavin.

3.1. Introduction:

Riboflavin (RF; Vitamin B_2) is a water-soluble vitamin that aids the breakdown of fats, proteins, ketone bodies, and carbohydrates into usable forms of energy for the human body.[1,2] Given its inability to be endogenously synthesized in humans, RF must be acquired through dietary sources, which accounts for its presence in a wide range of foods, including milk, cheese, fatty fish, meats, eggs, nuts, vegetables, whole-grain products, and certain fruits.[3,4] The optimum RF level is crucial for maintaining a healthy body. These include the proper functioning of the digestive system, and maintaining the health of multiple internal as well as external body parts such as the nerves, muscles, eyes, liver, etc. A deficiency of RF at the cellular level is known as ariboflavinosis and has been associated with various ailments such as anemia, mouth ulcers, fatigue, cracked lips, dry skin, cheilosis, throat pain, inhibited growth, tongue inflammation, conjunctivitis, etc.[5,6] In contrast, an excessive amount of RF poses a risk to human health as it can cause "oxidative damage to DNA and tissues when exposed to ultraviolet (UV) radiation".[7] This necessitates the need for a sensitive, efficient, accurate, and affordable method for quantitative and qualitative estimation of RF in food commodities, pharmaceutical, and clinical samples.

Electrochemical sensors offer cost-effective, quick, and on-site analysis of analytes. However, in order to increase the sensitivity and impart selectivity to the electrochemical sensors, careful choice of recognition element for electrode modification is needed.

Recently, graphitic carbon nitride (gCN) has garnered attention as a potential 2D material with diverse applications[8–11] owing to its remarkable characteristics, including favorable chemical stability, tremendous mechanical strength, larger surface area, notable adsorption capacity, catalytic activity, and environmental sustainability. However, gCN finds limited utility in electrochemical systems because of its compromised electrical

conductivity, hindered charge transfer, and insufficient solubility in solvents. The incorporation of metal oxides and gCN has the potential to stimulate the generation of delocalized electrons, which can improve the conductivity and can lead to several physicochemical advancements.[12] Amongst the various metal oxides, copper oxides are of specific interest. Copper(II) oxide (CuO) is classified as a p-type semiconductor with a very small band gap of 1.2 eV.[13] This material exhibits considerable potential for advancing electrochemical sensors owing to its notable electrochemical reactivity and capability to facilitate electron transfer reactions.[12] Interestingly, RF, being a biological chelating ligand, is known to have an affinity for complex formation with Cu(II) by coordinating through the electron-rich nitrogen and oxygen atoms on its structure.[14,15] Therefore, the CuO is specifically selected here for its bi-functional role: (i) to enhance the electrochemical performance of gCN by means of the interaction between the π-π electron cloud and with high spin density N of polymeric gCN structure and the vacant d orbitals of Cu(II);[16–18] and (ii) to take advantage of its selective interaction with RF to create a highly sensitive and selective sensor for RF detection in a complex matrix.

To the best of our knowledge, the electrodeposition of CuO.gCN composite has never been reported previously. Interestingly, only few papers (>10) demonstrates the use of bulk gCN.CuO for voltammetric sensing of analytes like dopamine, bisphenol, and p-nonylphenol. However, in all these publications, the material was immobilized using the drop-cast method, which doesn't offer any control over surface composition and morphology and suffers from poor stability. Furthermore, to date, the specific interaction of Cu(II) with RF has never been explored for its selective voltammetric estimation. Therefore, this article systematically describes the controlled electrodeposition of CuO.gCN composite on the electrode surface and its use for the electroanalysis of RF with exceptional sensitivity and selectivity.

3.2. Experimental:

3.2.1 Chemicals

All the AR grade chemicals were used for the synthesis and preparation of standard stock solutions and were obtained from CDH Fine Chemical. The chemicals were of high purity and thus were used without any further processing or purification. Throughout the experimental procedures, Milli-Q deionized water was utilized to prepare the standard solutions.

3.2.2 Synthesis Protocols

gCN was synthesized using melamine as the precursor following the previously reported method.[19] Briefly, melamine was heated at 600 °C for six hours. The temperature was achieved by increasing it at the rate of 6 °C/min. The process resulted in the synthesis of gCN, a yellow-coloured powder material. Next, the gCN.CuO composite was prepared by using the synthesized gCN along with CuAc. Precisely, 2g CuAc was thoroughly dissolved in 25 mL DI water. 0.5g of the synthesized gCN was suspended to the prepared solution while stirring. To this suspension, 20 mL of 1M NaOH solution was added dropwise while continuously stirring. The resulting 45 mL solution was subjected to 110 °C (achieved by increasing the temperature by 2 °C/min) for 2 hours in a Teflon-lined stainless steel autoclave. The synthesis protocol [20] resulted in a black precipitate, which was thoroughly rinsed with DI followed by drying at 60 °C. The material was referred as gCN.CuO and utilized for additional characterization.

3.2.3 Characterization details

The crystallographic data of the synthesized material was collected using a Rigaku miniflex 600 X-ray Diffractometer using a Cu-kα radiation source. The FT-IR spectroscopy was carried out using a Thermo Scientific TM Nicolet iD7 spectrometer in the wavenumber range of 450 – 4000 cm^{-1} with 4 cm^{-1} resolutions. The Nova Nano SEM

450 scanning electron microscope was employed to get surface and morphological data at 20kV. The XPS was performed using a Kα X-ray photoelectron spectrophotometer produced by Thermo Fisher Scientific. The device was outfitted with a micro-focused X-ray source that employed monochromatic Al Kα radiation, operating within an energy range spanning from 100 to 4000 eV.

3.2.4 Electrochemical Set-up

All the electrochemical measurements were carried out using PalmSens3. Ag/AgCl (3M KCl), 0.3 mm thick Pt wire and 3 mm glassy carbon (GCE) was used as reference, counter, & working electrode, respectively. Phosphate buffer solution (PB-7; pH-7.4) or 1 M potassium chloride was uses as supporting electrolyte.

3.2.5 Surface modified Electrode: Electrochemical synthesis of CuO nanoflakes decorated gCN

To carry out the electrodeposition of gCN.CuO, 10 mg of the prepared material was suspended in 10 mL of DI via ultrasonic agitation using a bath sonicator for 2 hours. The aliquot used for electrodeposition was formed by combining 1 mL of the prepared gCN.CuO suspension with 1 mL of PB-7 buffer solution in an electrochemical cell. Prior to electrodeposition, the GCE was mechanically polished using polishing kit, followed by an intensive rinsing with DI water. The electrodeposition was carried out using cyclic voltammetry (CV) as the experimental technique. The surface modification was achieved electrochemically by running the CV with The potential was scanned from E1 & Ei = -1.0 V to E2= +1.6 V, with a dE/dt = 100 $mV.s^{-1}$. The number of cycles (n_c) were optimized within the range of 15 to 40 to achieve the best performance. After the electrochemical surface modification, the modified electrode was cleaned with DI and left to dry under ambient condition. In the following text, the electrode that was electrodeposited will be referred to as gCN.CuO/GCE.

3.2.6 Electroanalytical Method

The optimized number of electrodeposition cycles was selected by comparing the electrochemical performance of the electrodes modified using different 'n_c'. To have a comparative assessment, the peak current of the modified electrode was measured for 500 µM potassium ferricyanide. The measurement was performed using CV and SWV with a dE/dt and frequency of 100 mV/s, and 10.0 Hz respectively, from Ei = -0.2 V to E2 = +0.6 V.

The electrodeposited surface suitability for voltammetric sensing applications was assessed using RF as the test analyte. A 1 mM RF stock solution was used for preparing the samples of different concentration following the dilution method. For electrochemical measurement, a 2 mL test solution was prepared using a fixed volume of PB-7, precisely 1 mL in all aliquots. For the calibration plot and detection of RF, Square wave voltammetry (SWV) was employed. The SWV settings were; potential window: -0.8 to 0 V; step size: 6 mV; amplitude: 25 mV; and frequency: 10.0 Hz.

3.2.7 Real sample preparation:

Almonds as a real sample

One almond equivalent to 1.086 g was taken and crushed using a mortar and pestle. The required consistency of paste was achieved by adding 2 mL of DI to the mortar pestle. The paste was collected as stock and used for making test samples. Two samples were prepared by taking 1 mL of the prepared paste to 1 mL of PB-7 and 800 µL of paste, 200 µL of DI water to 1 mL of PB-7.

Curd as a real sample

2 g of curd sample (85g pack, Misthi Doi, Mother Dairy Fruit & Vegetable Pvt. Ltd) was stirred using a vortex stirrer. The volume of the colloidal mixer was found to be nearly same as 2 mL. The prepared colloid was used to prepare the test solutions by mixing it

with PB-7 in 1:1 and 1:3 by volume. The volume of test samples was kept constant as 2 mL which contains 1 mL of PB-7 in all the samples.

Hershey's Shake as a real sample

The chocolate flavoured Hershey Shake (as purchased, 200 mL, Hershey's India Pvt. Ltd.) was diluted with the PB-7 for preparing three distinct sample solutions. Sample 1 consists of 250 µL of Hershey's shake in 1 mL of PB-7 and 750 µL DI, Sample 2 comprises 500 µL of Hershey's shake solution in 1 mL of PB-7 and 500 µL DI, and Sample 3 contains 1 mL of Hershey's shake solution in 1 mL of PB-7.

Becosules syrup as a real sample

The liquid Becosules syrup (Pfizer Ltd.) as purchased was used to prepare the test samples. As per the tabulated RF value, 5 mL of sample contains 2.54 mg of riboflavin sodium phosphate (molecular weight: 478.33 $gmol^{-1}$) which is equivalent to 1.06 mM solution. Considering the calculated molarity, three samples were prepared by keeping the volume of PB-7 constant (1 mL) and varying the volume of syrup to get the final concentration of 25, 40 and 80 µM, respectively. DI was used to keep the total volume constant as 4 mL.

Zincovit Tablet as a real sample

Each Zincovit tablet (Apex Laboratories Pvt Ltd) contains 1.6 mg of riboflavin as per the tabulated value. 2 tablet were therefore crushed and dissolved in 20 mL DI water to make a stock solution of 0.425 mM. Using the prepared stock solution, test samples of three different concentrations 20µM, 25µM, and 30µM, respectively were prepared. The test sample volume was maintained constant as 2 mL which had 1 mL as fixed volume of PB-7. The other 1 mL was made up of RF stock solution and DI.

Zincovit multivitamin tablet (Apex Laboratory Pvt. Ltd) and Becosules syrup (Pfizer Ltd.) were chosen as 2 pharmaceutical samples. Whereas almond, curd (85g pack, Misthi

Doi, Mother Dairy Fruit & Vegetable Pvt. Ltd), and chocolate flavored milk shake (200 mL, Hershey's India Pvt. Ltd.) were used as three food samples.

3.3. Results and Discussion

3.3.1 Material Characterization: Examining the gCN.CuO composites

Several characterization techniques were utilised for characterizing the synthesized gCN.CuO composites. To determine the crystallinity and composition of the gCN.CuO composite, X-ray diffraction analysis (XRD) was initially performed. The distinct diffraction patterns of the synthesized gCN and gCN.CuO composites are displayed in **Figure 3.1(a)**. The formation of gCN was confirmed from a clear peak at a 2θ value of 27.4° and a weak peak at a 2θ value of 13.1° in accordance with the XRD pattern of gCN reported previously.[21]

The synthesised gCN.CuO sample exhibits distinct XRD peaks corresponding to the distinctive diffraction patterns of gCN and CuO. The most prominent peaks at 2θ values of 35.7° and 38.8° correspond to the CuO crystal planes indexed as (002) and (111), respectively. The other peaks observed at 2θ values of 32.7°, 49.0°, 53.2°, 58.6°, 61.8°, 66.6°, 68.2°, 72.5°, and 75.1° can be attributed to the crystallographic planes of CuO, specifically the (-110), (112), (-202), (020), (202), (-113), (022), (220), and (311) planes, respectively. These planes are designated by an asterisk (∗). A standard JCPDS Card No. 45-0937 was used to index the peak corresponding to monoclinic CuO.[22] However, weak bumps at 2θ values of 27.4° and 13.1° correspond to the (100) and (002) crystal planes of gCN. The peaks exhibit diminished intensity compared to starting gCN, which can be explained based on its amorphous nature compared to the crystalline CuO.

FT-IR spectroscopy was next employed to study the compare the chemical bonds present in gCN and gCN.CuO. **Figure 3.1(b)** displays the FTIR spectra of both materials. The gCN spectrum displays a wide peak between 3100 and 3400 cm^{-1}, listing the "-NH" and

"-OH" groups of gCN. A number of peaks observed between 1100 and 1600 cm^{-1} arise because of C-N vibration arising from the gCN matrix. The peak at 1239 and 1317 cm^{-1} results from "C-N(-C)-C" or "C-NH-C". The sharp bands at 1640, 1569, and 1401 cm^{-1} have been ascribed to the aromatic "C–N" stretching vibration mode. The effective synthesis of gCN was further indicated by a sharp peak at 804 cm^{-1}. The FTIR spectrum of gCN.CuO composite shows two distinctive bands at 605.6 and 497.2 cm^{-1} in addition to the gCN peaks. These peaks correspond to the Bu mode of CuO. The "Cu-O" stretching vibration along the (101) direction may be attributed to the peak at 497.2 cm^{-1}, while the "Cu-O" stretching in the same direction can be explained by the high-frequency mode at 605.6 cm^{-1}. Furthermore, no other infrared active mode was detected in the 605–660 cm^{-1} range, thereby ruling out the presence of any additional phase, namely Cu_2O.[23] Therefore, both the XRD and FTIR investigations manifested the formation of gCN.CuO composite.

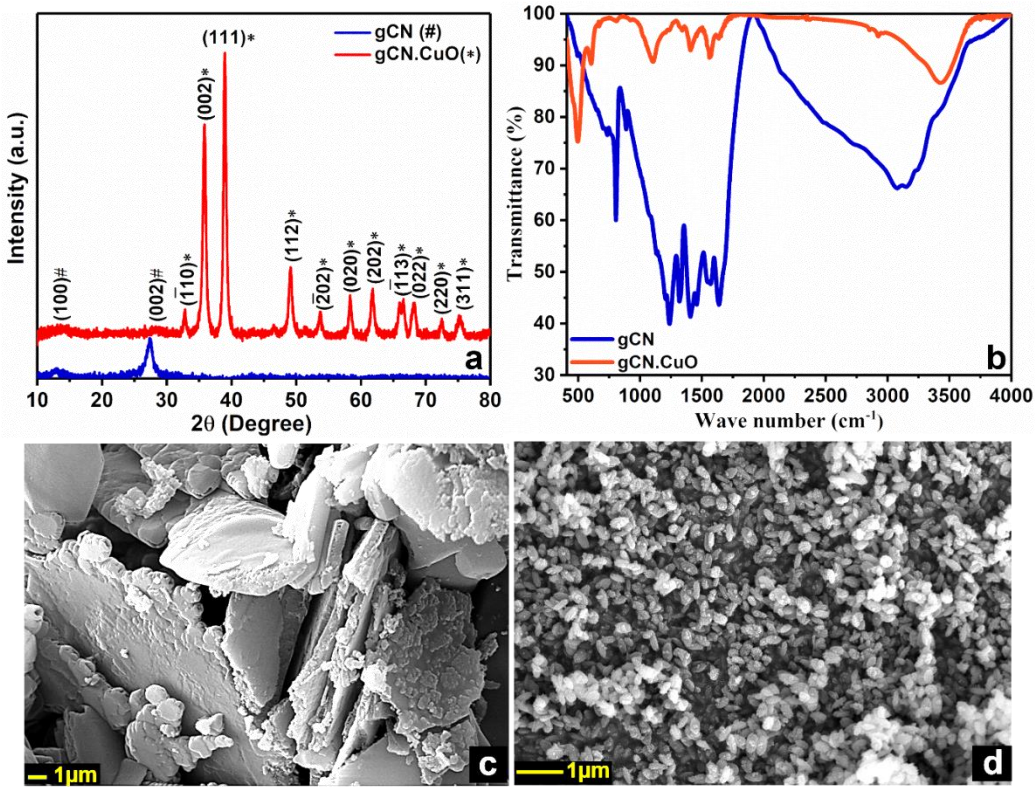

Figure 3.1: (a) Comparative XRD pattern, (b) Comparative FT-IR spectra of graphitic carbon nitride and its composite with CuO. (c) SEM image of synthesized graphitic carbon nitride (d) SEM images of graphitic carbon nitride-CuO composite.

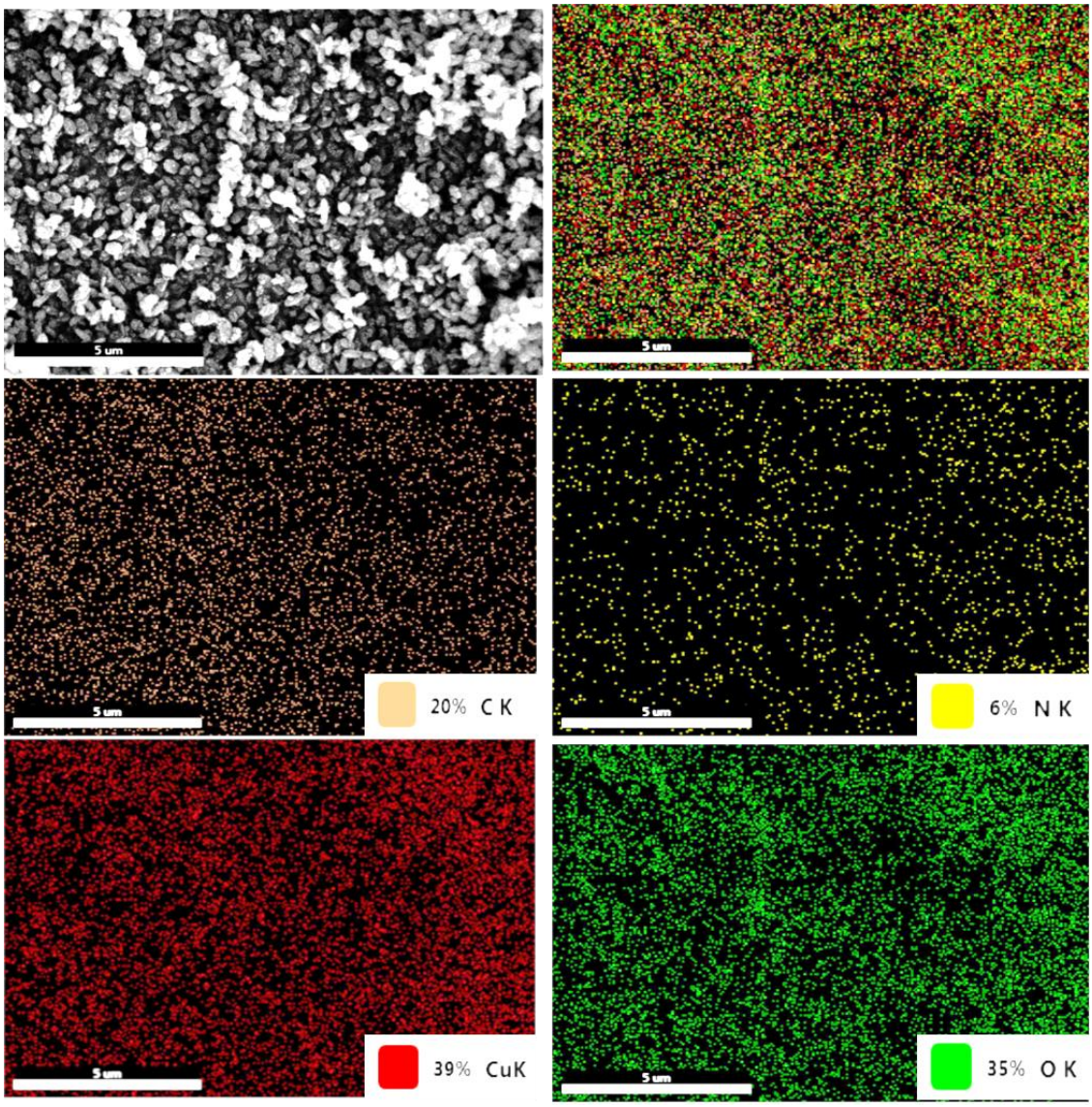

Figure 3.2: The surface elemental mapping of the as-synthesized gCN.CuO material.

After confirming the formation of gCN.CuO, the morphology and microstructure of the starting and prepared material were visualized using SEM. **Figure 3.1(c)** depicts a SEM picture of as-prepared gCN, revealing its layered structure mostly constituted of thin, micro-sized plate-like structures. Whereas the SEM of gCN.CuO (**Figure 3.1(d)**) revealed completely altered topography compared to the starting gCN. The SEM images demonstrated the formation of nanostructured CuO, which were found to be uniformly distributed over the sheet of gCN. The surface elemental analysis of the material using Energy-dispersive X-ray spectroscopy (**Figure 3.2**) quantified 33 atomic % of O and 35

atomic % of Cu, confirming the formation of CuO in agreement with the conclusions drawn from XRD and FTIR.

3.3.2 gCN.CuO electrodeposition and unveiling the underlying mechanism:

The experimental section provides a detailed account of the techniques employed for the electrodeposition utilizing the gCN.CuO composite. The cyclic voltammograms were observed for the electrodeposition of gCN.CuO is presented in (**Figure 3.3(a,b**)). The cyclic voltammograms exhibit electrochemical characteristics of both gCN and CuO. There exist three prominent peaks in the forward scan. The first peak observed at -0.08 V can be attributed to the oxidation process of Cu(0/I) to Cu(II).[24] The second peak corresponds to the electrochemical polymerization of the triazine ring, occurring at around +1.0 V. Subsequently, the third peak is indicative of the formation of radical cations, observed at +1.3 V.[19] Two well-known peaks were observed in the reverse cycle. The appearance of the peak in proximity to 0 V can be attributed to the reduction of Cu(II) to Cu(I), whereas the peak observed around -0.4 V is a result of the reduction of Cu(I) to Cu(0). Interestingly, the peak at +1.3 V was observed to increase with an increasing number of scans, which can be explained on the basis of the ability of Cu(II) to generate more radicals by its chemical reduction to Cu(I).[25,26] The generation of more and more radicals is expected to boost the electropolymerization of the triazine ring which is reflected by the increased current of polymerization peak at ~1.0 V. Due to the chemical reduction of Cu(II) to Cu(I) during free radical generation, the contribution of Cu(I) to Cu(0) becomes more prominent with increasing scans. Univocally, the cyclic voltammograms manifest the electrodeposition of gCN.CuO on the electrode surface provides a clear mechanistic signature of all the redox processes. Subsequently, the impact of surface modification on the electrochemical efficacy of the electrode was investigated.

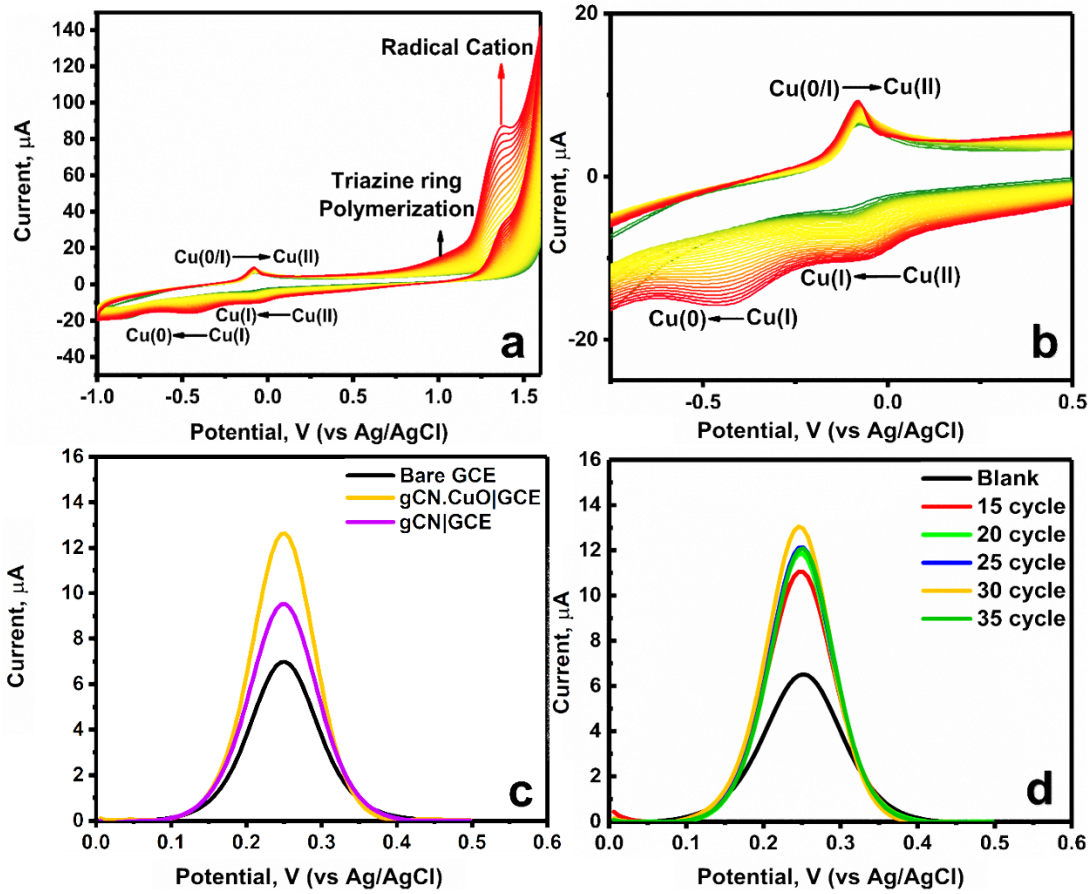

Figure 3.3: (a,b) Continuous CV curves recorded during electrodeposition of graphitic carbon nitride-CuO composite; Comparative SWV curves recorded using (c) bare GCE, gCN|GCE, and gCN.CuO|GCE; (d) gCN.CuO|GCE relating the variation in peak current of 500 µM potassium ferricyanide solution in response to surface modification and the number of electrodeposition scans.

Figure 3.3(c) illustrates the electrochemical response of $K_3[Fe(CN)_6]$ as observed using Bare GCE, gCN modified GCE, and gCN.CuO modified GCE. As depicted in the figure, both surface modifications led to enhanced peak current. However, it is noteworthy that the gCN.CuO modified GCE exhibited around two-fold current compared to the bare GCE. Therefore, the gCN.CuO electrodeposition process was thoroughly optimized in the subsequent sections.

3.3.2.1 Protocol Optimization

The perks of electrode modification are dependent on the thickness of the electrodeposited layer. Therefore, to achieve the desired electrochemical performance, it is necessary to optimize the thickness of the electrodeposited layers by adjusting the

electrodeposition parameters, specifically the solution concentrations and the number of scans. To do so, the electrodeposition was carried out using three different concentrations of gCN.CuO suspension. SWV profiles in the standard solution of $K_3[Fe(CN)_6]$ were recorded and analyzed to compare **Figure 3.3(d)** demonstrates the correlation between the number of scans (n) and corresponding changes in the peak current. A gradual increase in the peak current was observed when the deposition scans were increased till n = 30. Nevertheless, a minor decline in the current was witnessed for values of n greater than 30, which can be attributed to the formation of a thicker layer of gCN.CuO during electrodeposition. The presence of a thicker layer serves as a physical obstacle that impedes the movement of electrons from the working electrode to the analyte, hence inhibiting electron transfer. Hence, a solution concentration of 1mg/mL and a 30 electrodeposition scans were determined as the optimal parameters for the surface modification process. These parameters were employed for all subsequent experiments. **Figure 3.4** presents a comparative analysis of the electrochemical performance of three different configurations: bare, drop-casted, and electrofunctionalized gCN.CuO|GCE. The electro-functionalization process exhibited much greater peak currents in comparison to the drop-casting technique. The improved performance observed in this study can be attributed to the uniform surface modification via chemical/electrochemical processes, which allows for exact control over the thickness of the surface layer during the process of electro-functionalization. In contrast, drop casting suffers from agglomeration, non-uniform material loading, human error, and inadequate interfacial contact.[27,28] Moreover, the electrochemical and chemical redox processes during electrodeposition lead to several compositional and morphological changes in the composite material and the substrate, which can potentially affect the overall electrochemical performance of the surface-modified electrode.

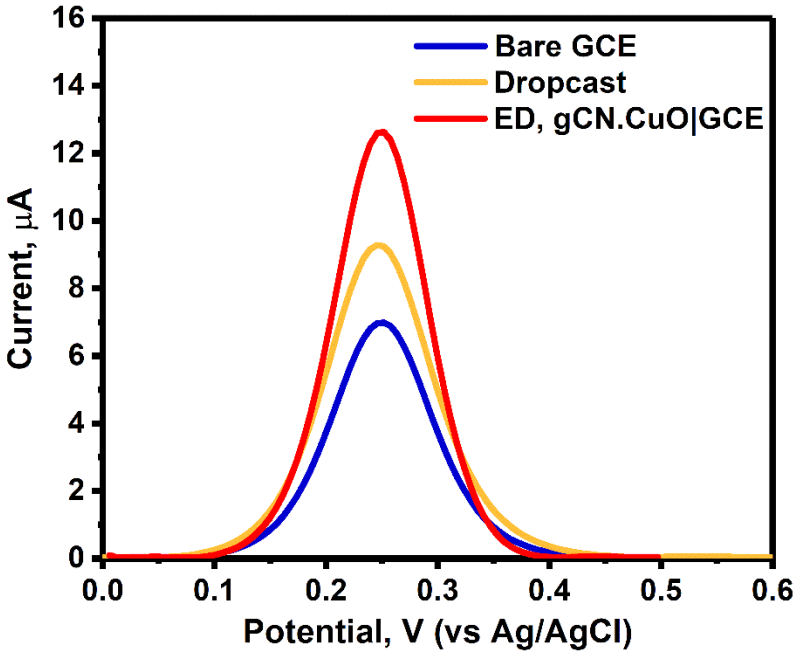

Figure 3.4: SWV curves of 500 µM potassium ferricyanide solution recorded using unmodified, drop-casted, and electrodeposited gCN.CuO|GCE

3.3.2.2 Surface Characterization

Next, the chemical and topographical changes brought by the electrodeposition protocol were extensively characterized. X-ray photoelectron spectroscopy was used in order to validate the structural characteristics, composite composition, and oxidation state of the elements that were present in the electrodeposited gCN.CuO composite. **Figure 3.5(a)** presents the high-resolution Cu2p spectrum of gCN.CuO|GCE. The two peaks at 933.1 eV and 953 eV corresponding to Cu $2p_{3/2}$ and Cu $2p_{1/2}$, respectively, highlights the presence of Cu^{2+} in the electrodeposited surface. The energy difference of 19.9 eV between the two peaks, caused by spin-orbit coupling, is in excellent accordance with previously reported data confirming the formation of CuO.[29] In addition, the two satellite peaks between 940-948 eV and 960-965 eV confirm the presence of Cu^{2+} with a $3d^9$ electron configuration in its ground state. These peaks are absent in the case of a completely filled $3d^{10}$ configuration of Cu^{+}, which provides further evidence that the electrodeposited layer consists of CuO.[30]

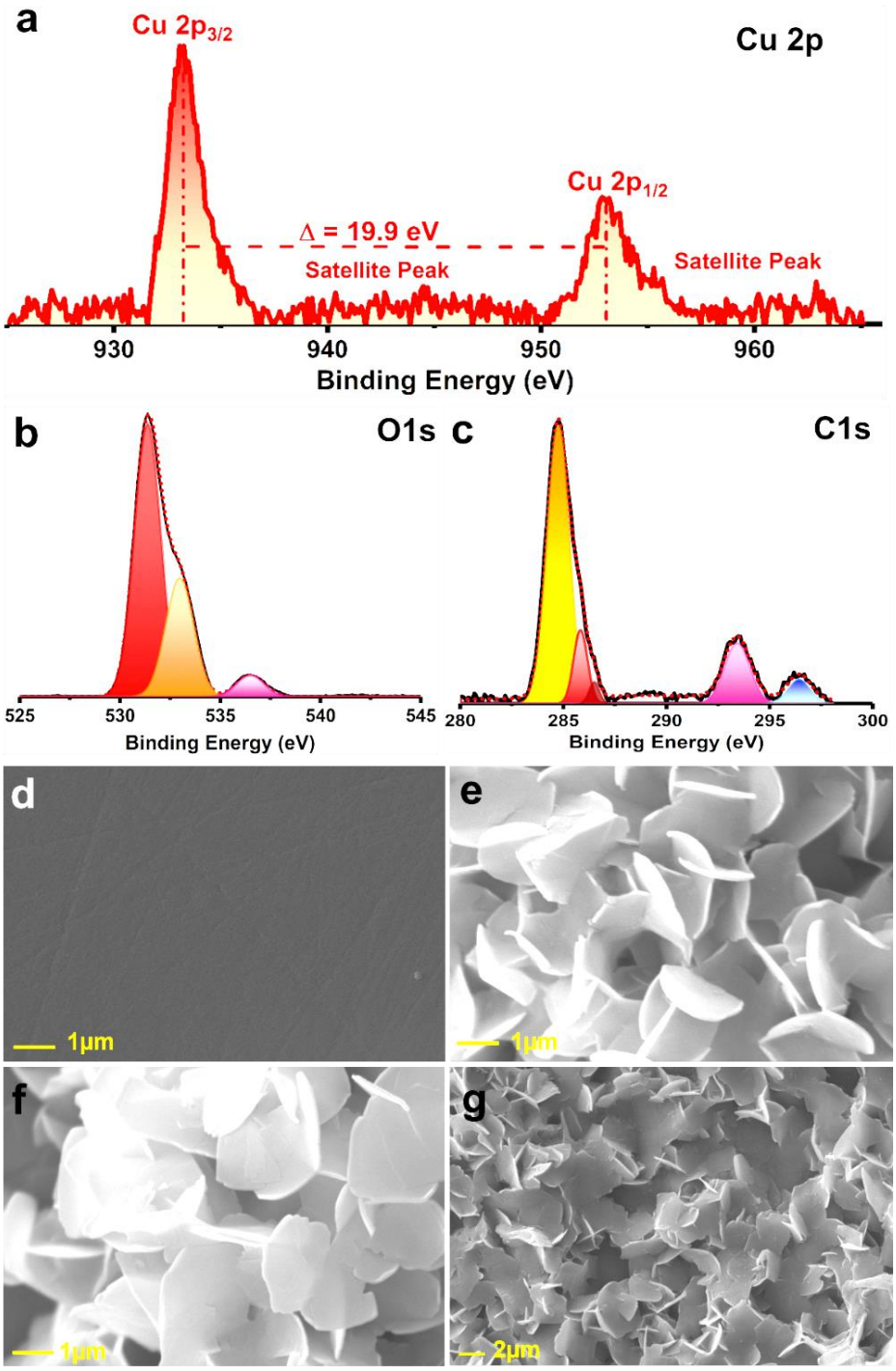

Figure 3.5: XPS spectrum of (a) Cu 2p; (b) O 1s; and (c) C 1s for gCN.CuO|GCE. HR-SEM image of (d) Bare GCE, and (e-g) gCN.CuO modified GCE (gCN.CuNF|GCE)

The presence of Cu-O was also concluded from the primary peak at 531.3 eV in the deconvoluted spectrum of O1s shown in **Figure 3.5(b)**. Interestingly the appearance of satellite peak at 536.4 eV in O1s spectrum hints towards the presence of π electrons in the composite as well as physiosorbed water and O_2.[31,32] It is to be noted that peak at BE

of 533 eV arises from the –C(O) functionalities of glassy carbon electrode and was also observed for the bare GCE.

Next, the C1s spectra was studied to detect the contribution of gCN in the electrodeposited layer (**Figure 3.5(c**)). The binding energies observed at 284.7 eV can be ascribed to the carbon-carbon coordination of the surface's adventitious carbon in gCN. The presence of sp^2-bonded carbon (N-CH=N) of the triazine ring was indicated by the peak at 285.8 eV. The weak peak observed at 286.5 eV is plausibly attributable to nitrogen-related defects that are present in the gCN system and are associated with the N-CH=N bonding within the system.[33] The two peaks in the extended C1s spectra correspond to the aromatic shake-up satellite peaks arising from the π cloud of polymeric triazine structures of gCN.[32,34,35] Therefore, the XPS analysis confirmed the effective electrodeposition of gCN.CuO layer on the GCE surface.

After characterizing the composition of the electrodeposited layer, further investigation was conducted to analyze its surface morphology and texture. Scanning electron microscopy (SEM) was first employed to visualise the topographical changes brought on by the electro-functionalization of the gCN.CuO composite. **Figure 3.5(d,e)** shows that electrodeposition process resulted in thin flake like structures uniformly decorating the GCE surface. These nanoflakes appeared all across the surface, and their sizes were rather uniform. Because of the nanoflake (NF) morphology of the electrodeposited surface, it is referred as gCN.CuNF/GCE.

The nanoflake morphology of gCN.CuNF|GCE is expected to augment the electrochemical charge transfer by providing a greater number of electroactive sites. Therefore, the electrochemical surface area (ECSA) of the modified and unmodified electrodes was calculated. In order to accomplish this, the variation of peak current as a function of increasing scan rate was investigated for both the unmodified GCE and the

gCN.CuNF|GCE using a known concentration of $K_3[Fe(CN)_6]$. The voltammograms and the observed linear relation are presented in **Figure 3.6(a,b)**. The ECSA of both the bare and gCN.CuNF|GCE electrode was determined by employing The Randles-Ševčík, taking into account a temperature of 25 °C.[36] ECSA of the GCE and gCN.CuNF|GCE was found to be 0.033 cm^2, and 0.04 cm^2, respectively. The 1.2 times larger surface area can be translated to the increased number of possible sites for interfacial electron transport explaining the increase in the current response observed after electrodeposition.

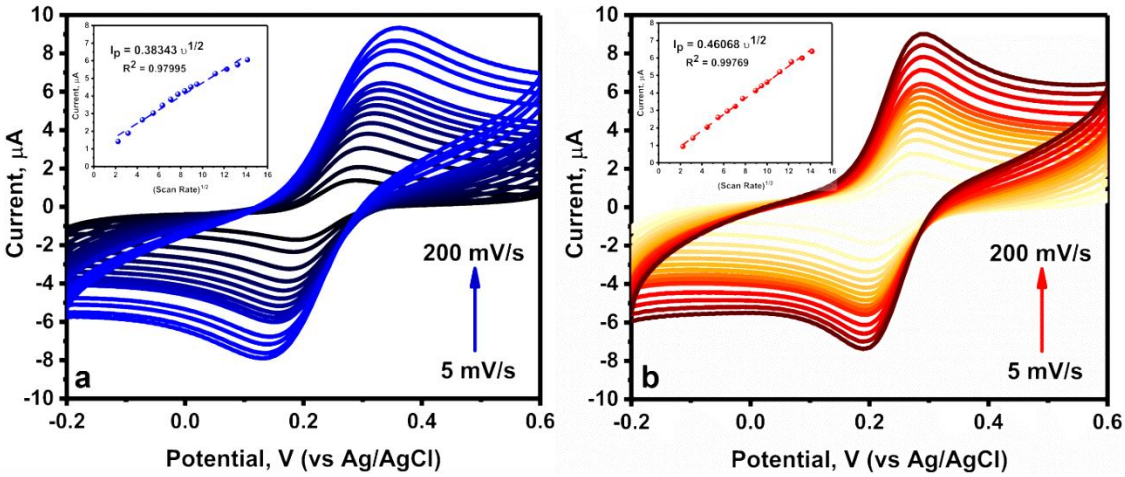

Figure 3.6: Cyclic voltammograms recorded in 500 µM potassium ferricyanide using (a) unmodified GCE and (b) gCN.CuNF|GCE as a function of different scan rate.

3.3.3 Analytical performance of modified electrode: Sensing of Riboflavin

From the extensive characterizations, it was inferred that the gCN.CuNF|GCE manifests significantly higher electrochemical activity and can lead to increase in sensitivity during electroanalysis. Therefore, the advantageous characteristics of gCN.CuNF|GCE was afterward utilized for the qualitative and quantitative analysis of Riboflavin (RF). **Figure 3.7(b)** illustrates the voltammograms acquired for a concentration of 100 µM RF using both the bare and modified GCE. On sweeping the potential from -0.6 V to 0.0 V, a sharp anodic peak at -0.405 V was observed which is reported to be associated with RF oxidation. The comparative SWV reveals the electro-functionalization of gCN.CuNF|GCE led to a current response approximately 4.6 times greater than that

observed with the bare GCE. In addition, the modified electrode exhibited a negative potential shift of approximately 13 mV compared to the bare electrode. It is important to mention that for $K_3[Fe(CN)_6]$ only a two-fold increase in peak current was observed without any measurable shift in peak potential. Therefore, the 4.6X higher current as well as significant peak shift clearly outlines that the modified electrode exhibits specific interactions with RF and enhanced electroactive area is not the sole factor responsible for the improved electrochemical performance. The selective interaction of Cu (II) (vacant d orbitals) with high spin density regions lying between N and O of RF molecule, as well as π-π interactions between the π conjugated gCN framework and RF molecules, are expected to contribute to the facilitated electron transfer and confers significantly higher electrochemical activity to the gCN.CuNF|GCE.[15,37]

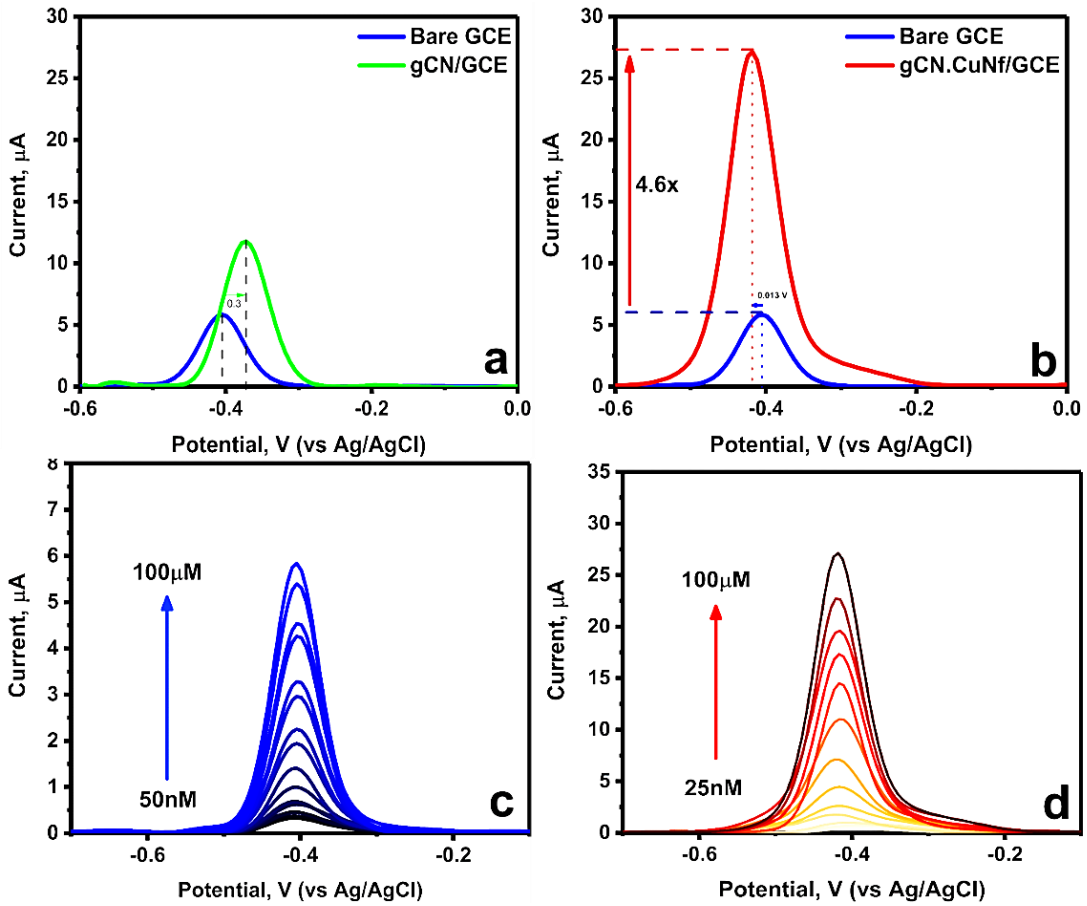

Figure 3.7: Comparative SWV curves recorded for 100 µM RF using (a) Bare GCE and gCN|GCE; (b) Bare GCE and gCN.CuNf|GCE. Concentration-dependent SWV curves were recorded in RF concentration ranging from 25 nM to 100 µM using (c) bare GCE and (d) gCN.CuNf|GCE.

Next, the peak current was monitored in response to the increasing concentration of RF peak. A gradually increasing peak current with increasing RF concentration for both electrodes is shown in **Figure 3.7(c-d)**. The peak potential remains constant hinting towards no charge transfer complications in the electrochemical process. From the linear calibration plots, it was observed that the increase in peak current was much more pronounced at lower concentrations, whereas, for concentration higher than 30 µM, a different slope was observed.

The correlation between the peak current and the RF concentration (**Figure 3.8)** can be expressed with the following linear equations:

$\boldsymbol{I_p}$ (μA) = 0.460 **C** [0.025-25 µM]; R^2 = 0.9911,

$\boldsymbol{I_p}$ (μA) = 0.172 **C** [30-100 µM] + 9.8419; R^2 = 0.9898……**:** gCN.CuNF|GCE

$\boldsymbol{I_p}$ (μA) = 0.111 **C** [0.05-40 µM]; R^2 = 0.9785,

$\boldsymbol{I_p}$ (μA) = 0.026 **C** [50-100 µM] + 3.2232 ; R^2 = 0.9811,……**:** Bare GCE

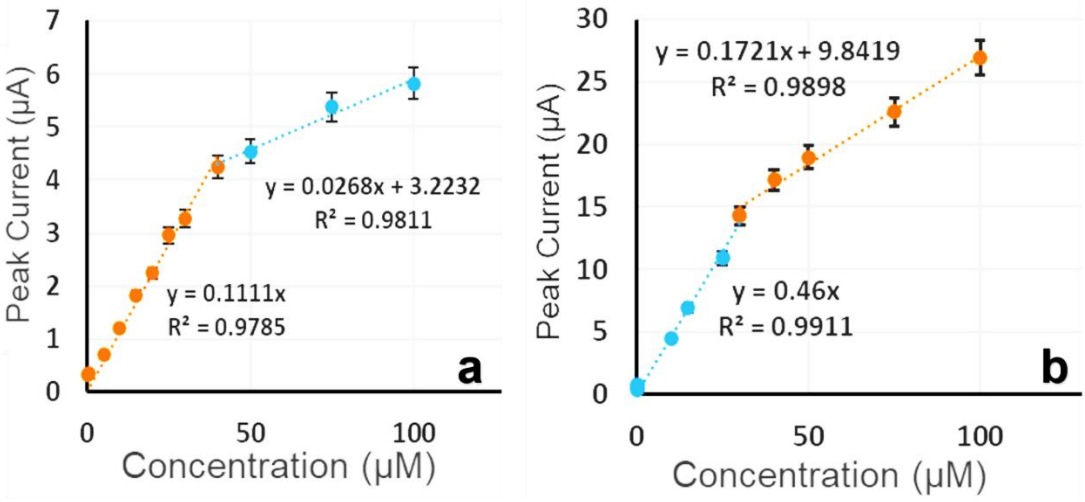

Figure 3.8: Calibration plot relating the peak current with the RF concentration recorded using (a) bare GCE, and (b) gCN.CuNF|GCE.

The slope of the linear regression equations of calibration parameter is a measure of sensitivity. It can be observed that the sensitivity of gCN.CuNF|GCE was approximately four times higher than that of bare electrode. The limit of detection (LOD) for the unmodified GCE was found to be 42 nM, whereas the gCN.CuNF|GCE showcased a

LOD of 6 nM. The improved level of sensitivity exhibited by the gCN.CuNF|GCE architecture underscores its significant utility in the realm of voltammetric sensing applications. The superior performance of the gCN.CuNF|GCE, in comparison to the previously reported sensors, has been outlined in ***Table 3.1***.

Table 3.1: Comparative performance analysis of the proposed sensor with the recently reported voltammetric sensors for RF estimation

Electroactive Surface	***Analytical Method***	***Conc. range (µM)***	***LOD (µM)***	***Modification method***	***Ref.***
Cr/SnO_2/GCE	DPV	0.2-1000	0.107	Drop cast	[38]
Bi_2O_3@MWCNT @g-C_3N_4/GCE	LSV	0.2-70	1.032	Drop cast	[39]
WO_3/TiO_2/Graphene/GCE	LSV	0.02-2.5	0.025	Drop cast	[40]
SnO_2-rGO/GCE	SWV	0.1-150	0.034	Drop cast	[41]
Poly(DL−phenylalanine)/CPE	DPV	6-30	0.092	Electrodeposition	[42]
MnO_2/GCE	DPV	2-110	0.027	Drop cast	[43]
gCN.CuNF|GCE	SWV	0.05-100	0.006	Single step electrodeposition	This work

3.3.4 Interference Study

Another crucial trait of a sensor is the ability to differentiate between the target analyte and interfering substances commonly present in the real, physiological and food samples. Therefore, the selectivity of the sensor was analysed by monitoring the deviation in the oxidation current observed for 1 µM RF solution at a peak potential of -0.4 V in a matrix having cyanocobalamin (B_{12}), ascorbic acid (AA), uric acid (UA), and hypoxanthine (HX) in addition to RF. It is evident from **Figure 3.9(a)** that no discernible change in the peak potential/current was observed even at higher concentration of interfering species. The results manifested the excellent selectivity of gCN.CuNF|GCE for assaying RF even in complicated matrices constituted of potentially similar chemical species.

3.3.5 Real Sample Study

Following the comprehensive qualitative and quantitative estimation of RF in test solutions, the practicality of the developed sensor was evaluated by estimating RF in real/commercial samples from the food and pharma industries. A detailed real sample preparation method for each of the chosen items is documented in the experimental section.

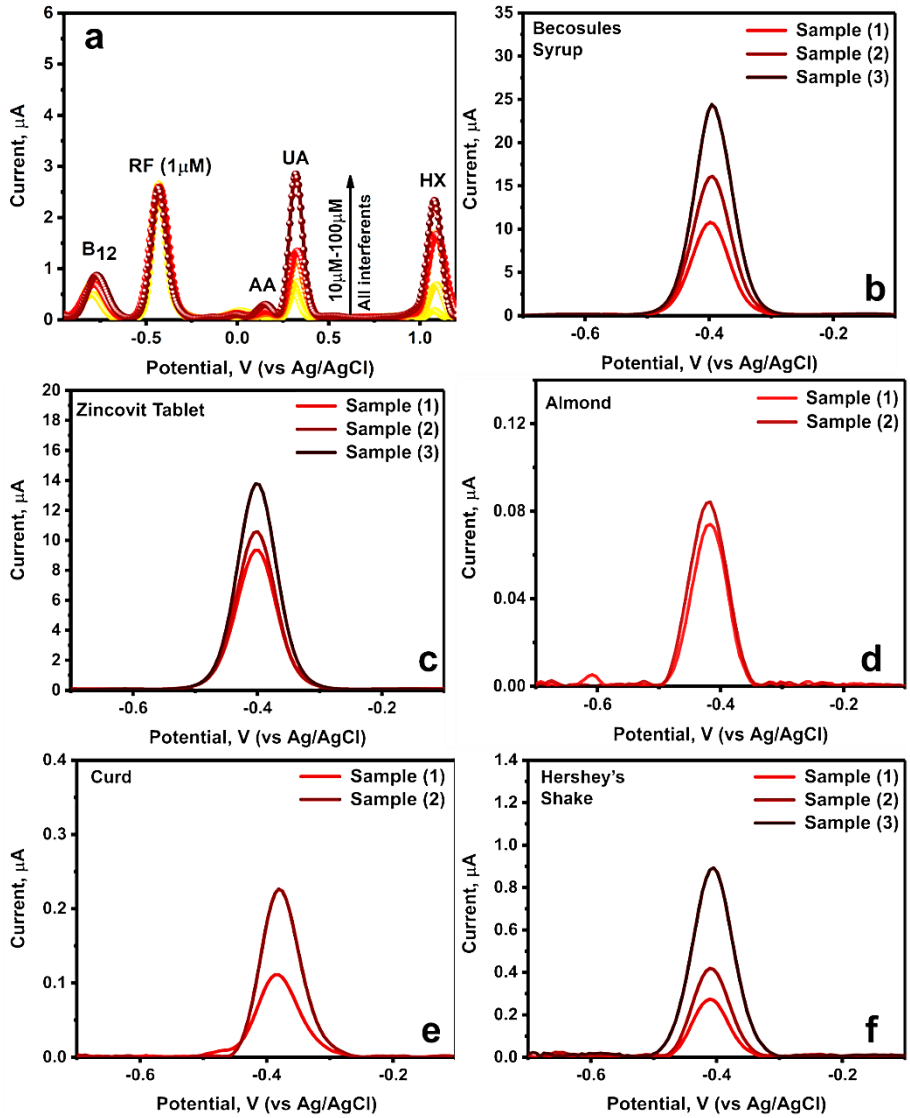

Figure 3.9: (a) Interference Study: SWV curves recorded in presence of 10 to 100 fold B12, AA UA, HX for RF using gCN.CuNF|GCE. (b-f) Real sample analysis: SWV demonstrating detection of RF in (b) Becosules Syrup, (c) Zincovit Tablet, (d) Almond, (e) Curd, and (f) Hershey's Shake.

The applicability of the sensor was first tested by validating the tabulated RF values of pharmaceutical samples. **Figure 3.9(b)** demonstrates the SWV recorded for test samples

prepared using commercial Becosules syrup. Each sample demonstrated a peak at -0.4 V, indicating the presence of RF. The peak current was found to increase with the increasing concentration of the prepared samples. The peak current was then used to quantify the RF in the test sample by employing the linear regression equation devised above. The results are presented in ***Table 3.2***. The data demonstrates a good agreement between the tabulated concentration and the detected values, with a maximum error of 5.76 %. A similar analysis of samples prepared using the Zincovit tablet was performed. The observed SWV are presented in **Figure 3.9(c)**, showcasing a sharp peak at -0.4 V, confirming the presence of RF in the tablet. The amount of riboflavin in the sample was determined by putting the measured current into the linear regression equation. The quantification data of the samples has been showcased in ***Table 3.2***.

Table 3.2: *Quantification of RF in real samples using gCN.CuNF|GCE.*

Sample	Current (µA)	Detected (µM)	Actual (µM)	Error (%)
Pfizer Becosules Syrup				
1	10.84	23.56	25	5.76
2	16.54	38.94	40	2.65
3	24.32	84.17	80	5.21
Zincovit Tablet				
1	9.34	20.30	20	1.50
2	10.67	23.19	25	7.24
3	13.96	30.35	30	1.16
Almond				
1	0.07	0.15	0.15	0.00
2	0.08	0.17	0.18	5.56
Curd				
1	0.11	0.24	0.25	4.00
2	0.22	0.48	0.46	4.35
Hershey's Shake				
1	0.26	0.57	0.55	3.64
2	0.42	0.91	0.94	3.19
3	0.89	1.94	1.96	1.02

Next, the presence of RF in food samples was quantified. The samples were prepared as mentioned in the experimental section. **Figure 3.9(d-f)** presents the square wave voltammogram recorded for Almond, Curd, and Milk Shake, respectively. All three

samples exhibit a discernible peak at around -0.4 V, which is ascribed to the presence of RF. Furthermore, the increase in peak current was observed upon spiking with RF stock solution, confirming the association of peak observed at -0.4V with the RF in the food samples. The results are presented in ***Table 3.2***. The observed peak current was then used to determine the amount of RF present in each sample. The observed values are tabulated in ***Table 3.2***. To validate the observed results, the amount of RF in samples was simultaneously quantified with direct UV-Vis analysis.[44] The study manifested excellent applicability of the developed electrochemical sensor for RF analysis in nutritional supplements and food samples.

3.3.6 Reliability Studies

To ensure the robustness of gCN.CuNF|GCE, the drop in electrochemical responses during continuous CV scans was monitored. **Figure 3.10 (a)** demonstrates that the gCN.CuNF|GCE manifests no measurable change in the blank response even after being subjected to 200 CV cycles. The fact that the blank voltammograms do not show any significant change demonstrates that the designed surface can withstand repeated measurements without any surface fouling. **Figure 3.10 (b)** illustrates the response of gCN.CuNF|GCE for first 100 SWV peak currents in 500 µM $K_3[Fe(CN)_6]$. After recording 100 consecutive readings, the peak current was found to drop by less than 5% of the initial current, as seen in the bar diagram. This indicates that the modified electrode exhibits appreciable level of stability for repetitive measurements.

The prolonged stability and durability of the designed interface were investigated by recording SWV response of $K_3[Fe(CN)_6]$, intermittently up to 30 days. The observations are depicted in **Figure 3.10 (c)**. As witnessed from the SW voltammograms, only a marginal drop in peak current was noticed after 21 days, even when the electrodes were stored in normal environmental conditions. The data indicates the remarkable stability of

the modified surface over a period of 30 days without any supplementary storage conditions. Nevertheless, the longevity of the electrodes can be prolonged by storing them in a dry atmosphere or a container filled with nitrogen. Next the reproducibility of the modification protocol was assessed by conducting experiments on three distinct GCE that were modified concurrently with gCN.CuNF. The current response of these electrodes was then measured in 500 µM $K_3[Fe(CN)_6]$ using Square Wave Voltammetry (SWV), and the results are depicted in **Figure 3.10 (d)**. The voltammograms showcase concordant peak currents and peak potentials demonstrating a satisfactory level of reproducibility of the proposed methodology.

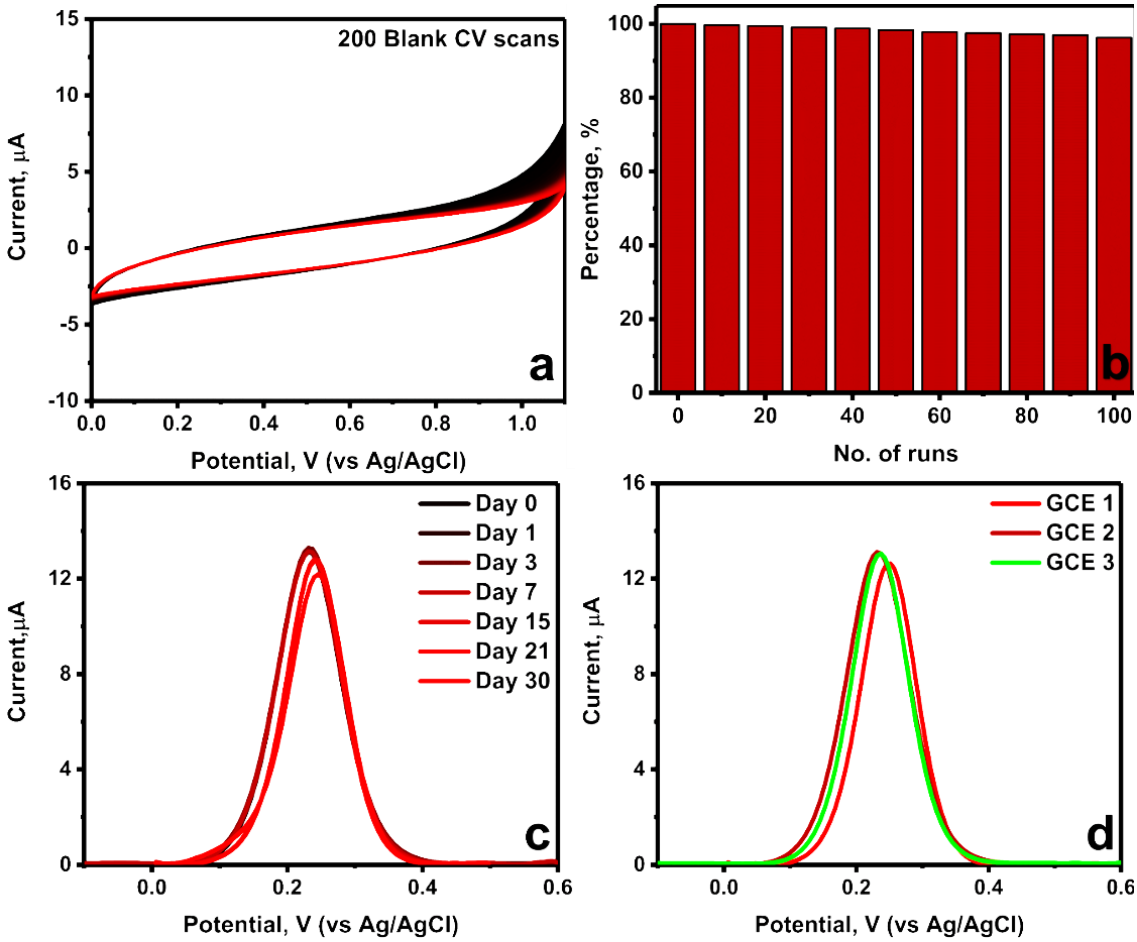

Figure 3.10: (a) 200 consecutive CV curves recorded in blank (pH 7, PB buffer) using gCN.CuNF|GCE; SWV responses recorded in 500 µM potassium ferricyanide solution representing variation in current: (b) for first 100 measurements (in percentage) (c) first 30 days (d) using three different GCE for modification.

3.4. Conclusions

In this study, electrodeposition of gCN.CuO nanoflakes (gCN.CuNF) directly on a glassy carbon electrode is presented. The synergistic role of both gCN and CuO demonstrated favorable properties for electroanalysis of RF ascribed to the selective interaction of Cu (II) (vacant d orbitals) with high spin density regions lying between N and O of RF molecule as well as π-π interactions between π conjugated gCN framework and RF molecules which are expected to contribute to the facilitated electron transfer and confer significantly higher electrochemical activity to the gCN.CuNF|GCE. Ascribed to the three-dimensional hierarchical framework, increased electroactive surface area as well as the greater number of interaction sites, the gCN.CuNF|GCE showcased a RF oxidation peak at -0.418 V with a 4.6 X higher current and a ~13 mV potential shift compared to bare GCE, indicating facilitated electro-oxidation at the modified electrode. The gCN.CuNF|GCE demonstrated a wider linear range from 25 nM to 100 µM with a LOD of 6 nM. The sensor manifested appreciable selectivity for RF detection as concluded from the unperturbed SWV signal corresponding to RF electro-oxidation in a complex matrix made up of several interfering species like cyanocobalamin (Vitamin B12). Furthermore, the proposed sensor was successful in validating RF levels in pharmaceutical formulations and food samples, showcasing an error percentage of > 7%. Showcasing appreciable stability, repeatability, and reproducibility, the proposed strategy outlines the benefits of electrodeposition of rationally chosen nanocomposite over conventional drop-cast methods for revolutionizing the selectivity and sensitivity of next-generation electrochemical sensors.

3.5. References:

(1) Huang, L.; Tian, S.; Zhao, W.; Liu, K.; Guo, J. Electrochemical Vitamin Sensors: A Critical Review. *Talanta* **2021**, *222*, 121645. https://doi.org/10.1016/j.talanta.2020.121645.

(2) Muthusankar, G.; Rajkumar, C.; Chen, S. M.; Karkuzhali, R.; Gopu, G.; Sangili, A.; Sengottuvelan, N.; Sankar, R. Sonochemical Driven Simple Preparation of Nitrogen-Doped Carbon Quantum Dots/SnO2 Nanocomposite: A Novel Electrocatalyst for Sensitive Voltammetric Determination of Riboflavin. *Sensors Actuators B Chem.* **2019**, *281*, 602–612. https://doi.org/10.1016/J.SNB.2018.10.145.

(3) Pinto, J. T.; Zempleni, J. Riboflavin. *Adv. Nutr.* **2016**, *7* (5), 973–975. https://doi.org/10.3945/an.116.012716.

(4) Powers, H. J. Riboflavin (Vitamin B-2) and Health. *Am. J. Clin. Nutr.* **2003**, *77* (6), 1352–1360. https://doi.org/10.1093/AJCN/77.6.1352.

(5) Phelps Brown, N. A.; Bron, A. J.; Harding, J. J.; Dewar, H. M. Nutrition Supplements and the Eye. *Eye 1998 121* **1998**, *12* (1), 127–133. https://doi.org/10.1038/eye.1998.21.

(6) Wahab, R.; Khan, F.; Alam, M.; Mishra, Y. K. Silver Nanoparticle Based Selective, Sensitive and Instantaneous Electrochemical Nanosensors for the Analysis of Riboflavin. *Mater. Sci. Semicond. Process.* **2023**, *153*, 107166. https://doi.org/10.1016/J.MSSP.2022.107166.

(7) Besaratinia, A.; Kim, S.-I.; Bates, S. E.; Pfeifer, G. P. Riboflavin Activated by Ultraviolet A1 Irradiation Induces Oxidative DNA Damage-Mediated Mutations Inhibited by Vitamin C. *Proc. Natl. Acad. Sci.* **2007**, *104* (14), 5953–5958. https://doi.org/10.1073/pnas.0610534104.

(8) Mishra, A.; Mehta, A.; Basu, S.; Shetti, N. P.; Reddy, K. R.; Aminabhavi, T. M. Graphitic Carbon Nitride (g–C3N4)–Based Metal-Free Photocatalysts for Water Splitting: A Review. *Carbon N. Y.* **2019**, *149*, 693–721. https://doi.org/10.1016/J.CARBON.2019.04.104.

(9) Li, Y.; Zhang, B.; Lü, H.-J.; Shen, M.; Zhang, L.; Shi, J. Converting CO2 into Fuels by Graphitic Carbon Nitride-Based Photocatalysts. *Nanotechnology* **2018**, *29* (41), 412001. https://doi.org/10.1088/1361-6528/AAD4C8.

(10) Chan, M. H.; Liu, R. S.; Hsiao, M. Graphitic Carbon Nitride-Based Nanocomposites and Their Biological Applications: A Review. *Nanoscale* **2019**, *11* (32), 14993–15003. https://doi.org/10.1039/C9NR04568F.

(11) Feng, L.; He, F.; Yang, G.; Gai, S.; Dai, Y.; Li, C.; Yang, P. NIR-Driven Graphitic-Phase Carbon Nitride Nanosheets for Efficient Bioimaging and Photodynamic Therapy. *J. Mater. Chem. B* **2016**, *4* (48), 8000–8008. https://doi.org/10.1039/C6TB02232D.

(12) Huang, Y.; Tan, Y.; Feng, C.; Wang, S.; Wu, H.; Zhang, G. Synthesis of CuO/g-C3N4 Composites, and Their Application to Voltammetric Sensing of Glucose and Dopamine. *Microchim. Acta* **2019**, *186* (1), 10. https://doi.org/10.1007/s00604-018-3120-z.

(13) Rakhshani, A. E. Preparation, Characteristics and Photovoltaic Properties of Cuprous Oxide—a Review. *Solid. State. Electron.* **1986**, *29* (1), 7–17. https://doi.org/10.1016/0038-1101(86)90191-7.

(14) Ahmad, I.; Anwar, Z.; Ahmed, S.; Sheraz, M. A.; Khattak, S. ur R. Metal Ion Mediated Photolysis Reactions of Riboflavin: A Kinetic Study. *J. Photochem. Photobiol. B Biol.* **2017**, *173*, 231–239. https://doi.org/10.1016/J.JPHOTOBIOL.2017.05.033.

(15) Jabbar, M. A.; Salahuddin, S.; Mannan, R. J.; Mahmood, A. J. Electrochemical Evidences for the Enhancement of Heterogeneous Electron Transfer Rates of Riboflavin in the Presence of Copper. *Dhaka Univ. J. Sci.* **2015**, *62* (2), 147–152. https://doi.org/10.3329/dujs.v62i2.21980.

(16) Zou, J.; Wu, S.; Liu, Y.; Sun, Y.; Cao, Y.; Hsu, J. P.; Shen Wee, A. T.; Jiang, J. An Ultra-Sensitive Electrochemical Sensor Based on 2D g-C3N4/CuO Nanocomposites for Dopamine Detection. *Carbon N. Y.* **2018**, *130*, 652–663. https://doi.org/10.1016/J.CARBON.2018.01.008.

(17) Zuo, S.; Li, D.; Yang, F.; Xu, H.; Huang, M.; Guan, Z.; Xia, D. Copper Oxide/Graphitic Carbon Nitride Composite for Bisphenol a Degradation by Boosted Peroxymonosulfate Activation: Mechanism of Cu-O Covalency Governs. *J. Colloid Interface Sci.* **2021**, *603*, 85–93. https://doi.org/10.1016/J.JCIS.2021.06.099.

(18) Atacan, K.; Özacar, M. Construction of a Non-Enzymatic Electrochemical Sensor Based on CuO/g-C3N4 Composite for Selective Detection of Hydrogen Peroxide. *Mater. Chem. Phys.* **2021**, *266*. https://doi.org/10.1016/J.MATCHEMPHYS.2021.124527.

(19) Singh, A. K.; Keshari, P.; Saroj, A.; Ramanathan, V.; Rosy. Electrodeposition of Graphitic Carbon Nitride and Its In Situ Decoration with MnO2 Nanostructures: A Tailored Interface for Dopamine Sensing. *Surfaces and Interfaces* **2023**, *42*, 103316. https://doi.org/10.1016/j.surfin.2023.103316.

(20) Jiang, T.; Wang, Y.; Meng, D.; Wu, X.; Wang, J.; Chen, J. Controllable Fabrication of CuO Nanostructure by Hydrothermal Method and Its Properties. *Appl. Surf. Sci.* **2014**, *311*, 602–608. https://doi.org/10.1016/J.APSUSC.2014.05.116.

(21) Kumar Singh, A.; Das, C.; Indra, A. Scope and Prospect of Transition Metal-Based Cocatalysts for Visible Light-Driven Photocatalytic Hydrogen Evolution with Graphitic Carbon Nitride. *Coord. Chem. Rev.* **2022**, *465*, 214516. https://doi.org/10.1016/J.CCR.2022.214516.

(22) Bhuvaneshwari, S.; Gopalakrishnan, N. Hydrothermally Synthesized Copper Oxide (CuO) Superstructures for Ammonia Sensing. *J. Colloid Interface Sci.* **2016**, *480*, 76–84. https://doi.org/10.1016/J.JCIS.2016.07.004.

(23) Ethiraj, A. S.; Kang, D. J. Synthesis and Characterization of CuO Nanowires by a Simple Wet Chemical Method. *Nanoscale Res. Lett.* **2012**, *7* (1), 70. https://doi.org/10.1186/1556-276X-7-70.

(24) Scherzer, M.; Girgsdies, F.; Stotz, E.; Willinger, M.-G.; Frei, E.; Schlögl, R.; Pietsch, U.; Lunkenbein, T. Electrochemical Surface Oxidation of Copper Studied by in Situ Grazing Incidence X-Ray Diffraction. *J. Phys. Chem. C* **2019**, *123* (21), 13253–13262. https://doi.org/10.1021/acs.jpcc.9b00282.

(25) Dellinger, B.; Lomnicki, S.; Khachatryan, L.; Maskos, Z.; Hall, R. W.; Adounkpe, J.; McFerrin, C.; Truong, H. Formation and Stabilization of Persistent Free Radicals. *Proc. Combust. Inst.* **2007**, *31* (1), 521–528. https://doi.org/10.1016/J.PROCI.2006.07.172.

(26) Nayak, R.; Ali, F. A.; Mishra, D. K.; Ray, D.; Aswal, V. K.; Sahoo, S. K.; Nanda, B. Fabrication of CuO Nanoparticle: An Efficient Catalyst Utilized for Sensing and Degradation of Phenol. *J. Mater. Res. Technol.* **2020**, *9* (5), 11045–11059. https://doi.org/10.1016/J.JMRT.2020.07.100.

(27) Kaliyaraj Selva Kumar, A.; Zhang, Y.; Li, D.; Compton, R. G. A Mini-Review: How Reliable Is the Drop Casting Technique? *Electrochem. commun.* **2020**, *121*, 106867. https://doi.org/10.1016/J.ELECOM.2020.106867.

(28) Dr. Wajiha Abbasi, P. D. L. L. Electrode Modification Through Chemical and Electrochemical Deposition of Polytyramine Film for Biosensing Application. *Int. J. Eng. Res. Technol.* **2015**, *4* (6), 427–433.

(29) Siddiqui, H.; Qureshi, M. S.; Zia Haque, F. Biosynthesis of Flower-Shaped CuO Nanostructures and Their Photocatalytic and Antibacterial Activities. *Nano-Micro Lett.* **123AD**, *12*. https://doi.org/10.1007/s40820-019-0357-y.

(30) Devaraj, M.; Deivasigamani, R. K.; Jeyadevan, S. Enhancement of the Electrochemical Behavior of CuO Nanoleaves on MWCNTs/GC Composite Film Modified Electrode for Determination of Norfloxacin. *Colloids Surfaces B Biointerfaces* **2013**, *102*, 554–561. https://doi.org/10.1016/J.COLSURFB.2012.08.051.

(31) Chowdhury, F. A.; Hossain, M. A.; Uchida, K.; Tamura, T.; Sugawa, K.; Mochida, T.; Otsuki, J.; Mohiuddin, T.; Boby, M. A.; Alam, M. S. Graphene Oxide/Carbon Nanoparticle Thin Film Based IR Detector: Surface Properties and Device Characterization. *AIP Adv.* **2015**, *5* (10). https://doi.org/10.1063/1.4935042.

(32) Gengenbach, T. R.; Major, G. H.; Linford, M. R.; Easton, C. D. Practical Guides for X-Ray Photoelectron Spectroscopy (XPS): Interpreting the Carbon 1s Spectrum. *J. Vac. Sci. Technol. A Vacuum, Surfaces, Film.* **2021**, *39* (1), 13204. https://doi.org/10.1116/6.0000682.

(33) Choudhury, B.; Paul, K. K.; Sanyal, D.; Hazarika, A.; Giri, P. K. Evolution of Nitrogen-Related Defects in Graphitic Carbon Nitride Nanosheets Probed by Positron Annihilation and Photoluminescence Spectroscopy. *J. Phys. Chem. C* **2018**, *122* (16), 9209–9219. https://doi.org/10.1021/acs.jpcc.8b01388.

(34) Alwin, E.; Nowicki, W.; Wojcieszak, R.; Zieliński, M.; Pietrowski, M. Elucidating the Structure of the Graphitic Carbon Nitride Nanomaterials via X-Ray

Photoelectron Spectroscopy and X-Ray Powder Diffraction Techniques. *Dalt. Trans.* **2020**, *49* (36), 12805–12813. https://doi.org/10.1039/d0dt02325f.

(35) Majumdar, A.; Das, S. C.; Shripathi, T.; Heinicke, J.; Hippler, R. Shake up Satellites and Fluorescence Property of Carbon Nitride and Hydrogenated Carbon Nitride: Annealing Effect. *Surf. Sci.* **2013**, *609*, 53–61. https://doi.org/10.1016/J.SUSC.2012.11.003.

(36) Yadav, K.; Garg, S.; Singh, A. K.; Singh, S.; Singh Parmar, A.; Rosy. Protein Nano Dots Conjugated AuNP, Poly-Lysine Biointerface for the Selective Voltammetric Estimation of Melatonin in Pharmaceutical and Food Samples. *Microchem. J.* **2022**, *179*, 107563. https://doi.org/10.1016/j.microc.2022.107563.

(37) Maiti, S.; Barman, G.; Konar Laha, J. Detection of Heavy Metals (Cu+2, Hg+2) by Biosynthesized Silver Nanoparticles. *Appl. Nanosci.* **2016**, *6* (4), 529–538. https://doi.org/10.1007/s13204-015-0452-4.

(38) Lavanya, N.; Radhakrishnan, S.; Sekar, C.; Navaneethan, M.; Hayakawa, Y. Fabrication of Cr Doped SnO2 Nanoparticles Based Biosensor for the Selective Determination of Riboflavin in Pharmaceuticals. *Analyst* **2013**, *138* (7), 2061–2067. https://doi.org/10.1039/C3AN36754A.

(39) Kapoor, A.; Varnika; Pratibha; Rajput, J. K.; Singh, D.; Kumar, N.; Jigyasa. Bi2O3@MWCNT@g-C3N4 Ternary Nanocomposite for the Efficient Electrochemical Determination of Riboflavin in Pharmaceutical Samples. *J. Food Compos. Anal.* **2022**, *114*, 104792. https://doi.org/10.1016/J.JFCA.2022.104792.

(40) Grace, A. A.; Thillaiarasi, S.; Dharuman, V. Binary Metal Oxide Adsorbed Graphene Modified Glassy Carbon Electrode for Detection of Riboflavin. *Electroanalysis* **2021**, *33* (4), 993–1006. https://doi.org/10.1002/ELAN.202060429.

(41) Sriramprabha, R.; Divagar, M.; Ponpandian, N.; Viswanathan, C. Tin Oxide/Reduced Graphene Oxide Nanocomposite-Modified Electrode for Selective and Sensitive Detection of Riboflavin. *J. Electrochem. Soc.* **2018**, *165* (11), B498–B507. https://doi.org/10.1149/2.0761811jes.

(42) Hareesha, N.; Manjunatha, J. G. A Simple and Low-Cost Poly (Dl-Phenylalanine) Modified Carbon Sensor for the Improved Electrochemical Analysis of Riboflavin. *J. Sci. Adv. Mater. Devices* **2020**, *5* (4), 502–511. https://doi.org/10.1016/J.JSAMD.2020.08.005.

(43) Huang, D.-Q.; Wu, H.; Song, C.; Zhu, Q.; Zhang, H.; Sheng, L.-Q.; Xu, H.-J.; Liu, Z.-D. The Determination of Riboflavin (Vitamin B 2) Using Manganese Dioxide Modified Glassy Carbon Electrode by Differential Pulse Voltammetry. *Int. J. Electrochem. Sci* **2018**, *13*, 8303–8312. https://doi.org/10.20964/2018.09.02.

(44) Mokhtari, P.; Ghaedi, M. Water Compatible Molecularly Imprinted Polymer for Controlled Release of Riboflavin as Drug Delivery System. *Eur. Polym. J.* **2019**, *118*, 614–618. https://doi.org/10.1016/j.eurpolymj.2019.06.038.